A COMPUTATIONAL MODEL OF THE HAMMOND ORGAN VIBRATO/CHORUS USING WAVE DIGITAL FILTERS

Kurt James Werner, W. Ross Dunkel, and François G. Germain

Center for Computer Research in Music and Acoustics (CCRMA), Stanford University
660 Lomita Drive, Stanford, CA 94305, USA
[kwerner, chigi22, francois]@ccrma.stanford.edu

ABSTRACT

We present a computational model of the Hammond tonewheel organ vibrato/chorus, a musical audio effect comprising an LC ladder circuit and an electromechanical scanner. We model the LC ladder using the Wave Digital Filter (WDF) formalism, and introduce a new approach to resolving multiple nonadaptable linear elements at the root of a WDF tree. Additionally we formalize how to apply the well-known warped Bilinear Transform to WDF discretization of capacitors and inductors and review WDF polarity inverters. To model the scanner we propose a simplified and physically-informed approach. We discuss the time- and frequency-domain behavior of the model, emphasizing the spectral properties of interpolation between the taps of the LC ladder.

1. INTRODUCTION

The Hammond tonewheel organ's vibrato/chorus[1] (Fig. 1, Table 1) is a crucial ingredient of its unique sound. Its sonic character is highly valued by musicians, having even been made into a guitar effect [2]. The vibrato/chorus consists of an LC ladder circuit (Fig. 1) and an electromechanical "scanner" [3], with three user-selectable "vibrato" (V1, V2, V3) and "chorus" (C1, C2, C3) settings. In this paper, we introduce a model of the Hammond organ vibrato/chorus comprising a Wave Digital Filter (WDF) [4] model of the LC ladder circuit and a simplified model of the scanner.

WDF theory was originally developed to facilitate the design of digital filters based on analog ladder prototypes [5]. In that context, the low coefficient sensitivity of these prototypes leads to attractive numerical properties in the WDF. Recent years have seen an expansion of the use of WDFs into new fields including virtual analog circuit modeling [6]. Interestingly, ladder topologies also show up in electro-mechanical equivalent circuit models of the torsional modes of spring vibration relevant to spring reverb units [7], another effect common in Hammond organs.

Modeling the Hammond organ LC ladder as a WDF presents an issue that suggests an extension to WDF theory, and an opportunity to discuss finer points of polarity handling and reactance discretization. First, the ladder circuit has two non-adaptable linear elements (a voltage source and a switch), one more than classical WDF methods can handle. To address this, we extend the method of [8] to the case of multiple linear nonadaptable elements at the root of a WDF tree. Second, the circuit's 36 reactances create magnitude responses with numerous salient features. We apply the well-known frequency-warped bilinear transform to the wave-digital capacitor and inductor to help control magnitude response matching. Finally, polarity bookkeeping of port connections and the 19 outputs of the LC ladder is non-trivial. Since it is essential

to get each port's polarity correct and to simplify the calculation of node voltages, we review the derivation of wave-digital polarity inverters and illustrate their systematic use.

Although the vibrato/chorus has not been studied in the virtual analog context, there exists extensive related work on modeling other aspects of the complex and pleasingly idiosyncratic sound of the Hammond organ. For the practicing musician, a series of five Sound on Sound articles (beginning with [9]) details how to mimic each sub-system of the Hammond from tonewheel to Leslie speaker using standard synthesis tools. [10] points out the difficulty of emulating the vibrato/chorus using a standard digital chorus. Numerous commercial emulations known as "clonewheel organs" have been released over the years. Academic papers have covered various aspects of the Hammond sound. Pekonen *et al.* [11] propose efficient models of the organ's basic apparatus including tonewheels draw-bars. More abstractly, a novel "Hammondizer" effect by Werner and Abel [12] imprints the sonic characteristics of the organ onto any input audio, extending effect processing [13] within a modal reverberator framework [14]. An important part of the organ's sound, the Leslie rotating speaker [15] has been the subject of the majority of Hammond-related academic work. Its simulation has been tackled using a perceptual approach [16], modulated and interpolated delay lines [17,18][2], Doppler shift and amplitude modulation [19, 20], a measurement-based black box approach [21], and spectral delay filters [11].

The paper is structured as follows. Section 2 details the Hammond vibrato/chorus. Section 3 presents a simplified model of the scanner. Section 4 presents a WDF model of the LC ladder circuit. Section 5 characterizes these models.

2. REFERENCE SYSTEM DESCRIPTION

This section details the Hammond Organ vibrato/chorus, which includes a LC ladder circuit (Fig. 1, bottom, Section 2.1) and an electromechanical "scanner" apparatus (Fig. 1, top, Section 2.2). The gray box on Fig. 1 represents a bank of switches that connect the tap node voltages $v_1 \cdots v_{19}$ on the ladder to the terminals $t_1 \cdots t_9$ on the scanner. The setting (V1/V2/V3/C1/C2/C3) controls these switches according to Table 2.

In principle, the LC ladder serves the same purpose as the delay line in a standard digital chorus effect [22]. The LC ladder differs from a delay line in that the LC ladder is not strictly unidirectional and that it filters as it delays a signal. This filtering features pronounced non-uniform passband ripples and a lowpass cutoff that depends on the inductor and capacitor values.

On the other hand, the scanner serves the same purpose as interpolation in a standard digital modulated-delay effect [22]. Stan-

---

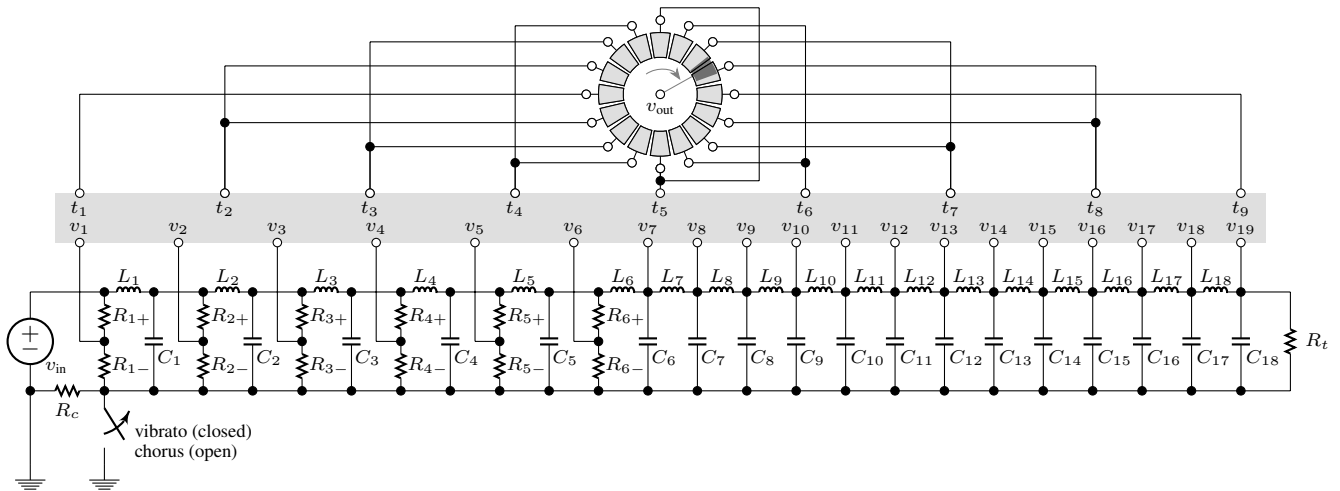[1]We study the version used in late-model Hammond B-3s [1]

[2]https://ccrma.stanford.edu/ jos/pasp/Leslie.html

Figure 1: *Vibrato/Chorus Schematic.*
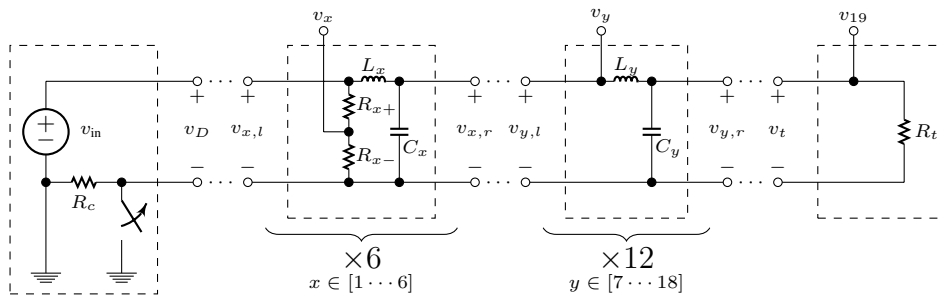
Figure 2: *Vibrato/Chorus Schematic Partitioned.*

Table 1: *Component values.*

Name	value	units
R_c	22	kΩ
R_{1+}	27	kΩ
R_{1-}	68	kΩ
R_{2+}	56	kΩ
R_{3+}	39	kΩ
R_{2-}, R_{3-}	0.15	MΩ
R_{4+}	33	kΩ
R_{5+}	18	kΩ
R_{6+}	12	kΩ
$R_{4-} \cdots R_{6-}$	0.18	MΩ
$L_1 \cdots L_{18}$	500	mH
$C_1 \cdots C_{17}$	0.004	μF
C_{18}	0.001	μF
R_t	15	kΩ

dard digital linear interpolation has a well-known lowpass characteristic [18][3] that digital audio effect designers often try to avoid by using, e.g., allpass interpolation [18][4]. Ironically, the scanner of the Hammond Organ vibrato/chorus essentially implements linear interpolation—meaning it does *not* have an allpass characteristic.

Table 2: *Taps for different depth settings.*

depth	t_1	t_2	t_3	t_4	t_5	t_6	t_7	t_8	t_9
V1/C1	v_1	v_2	v_3	v_4	v_5	v_6	v_7	v_8	v_9
V2/C2	v_1	v_2	v_3	v_5	v_7	v_9	v_{11}	v_{12}	v_{13}
V3/C3	v_1	v_2	v_4	v_7	v_{10}	v_{13}	v_{16}	v_{18}	v_{19}

2.1. LC Ladder Circuit

The input signal is represented as an ideal voltage source v_{in}. 19 LC ladder stages are composed of inductors $L_1 \cdots L_{19}$, capacitors $C_1 \cdots C_{19}$, and voltage divider pairs R_{k+} and R_{k-}, $k \in [1 \cdots 6]$. A termination resistor R_t ends the ladder. A switch controls whether R_c is shorted or not. Electrical component values for the circuit are given in Table 1 [1].

---

[3]https://ccrma.stanford.edu/~jos/pasp/
Fractional_Delay_Filtering_Linear.html
[4]https://ccrma.stanford.edu/~jos/pasp/First_
Order_Allpass_Interpolation.html

This highly structured circuit is partitioned into four subcircuits as shown in Fig. 2. The first subcircuit includes v_{in}, R_c, and the switch and presents a port "D" to the rest of the circuit.

The second subcircuit has 6 stages indexed by $x \in [1 \cdots 6]$: inductor L_x, capacitor C_x, and voltage divider pair R_{x+} and R_{x-}. The tap node voltage v_x is the output of each stage. Each stage presents a left-facing ("x, l") and right-facing ("x, r") port to the rest of the circuit. Ports "D" and "$1, l$" are connected and the 5 port pairs "$(k + 1), l$" and "k, r", $k \in [2 \cdots 6]$ are connected.

The third subcircuit has 12 stages indexed by $y \in [7 \cdots 18]$: inductor L_y and capacitor C_y. The tap node voltage v_y is the output of each stage. Each stage presents a left-facing ("y, l") and right-facing ("y, r") port to the rest of the circuit. Ports "$6, r$" and "$7, l$" are connected and the 11 port pairs "$(k + 1), l$" and "k, r", $k \in [7 \cdots 17]$ are connected.

The fourth subcircuit is simply the termination resistance R_t that presents port t to the rest of the circuit and has the tap node voltage v_{19} as an output. Ports "$18, r$" and "t" are connected.

2.2. Scanner Device

The vibrato scanner consists of a moving rotor with node voltage v_{out} that cyclically scans a stack of keystone-shaped output plates across 16 fixed stacks of identical plates arranged in a circle. At any given time, 2 of these 16 stacks partially overlap the rotor stack, forming two capacitors whose capacitances are pro-
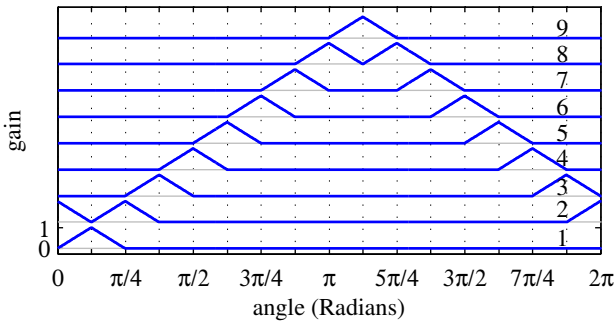
Figure 3: *Gain applied to each scanner terminal $t_1 \cdots t_9$.*

portional to the overlapping area between each fixed stack and the rotor stack. Conceptually, these two capacitances form a time-varying capacitive voltage divider, which crossfades between the node voltages of these 2 stacks. The 16 fixed plate stacks are connected to the 9 terminals $t_1 \cdots t_9$ which sets their respective node voltages to the node voltages of the corresponding terminals. As the rotor undergoes a complete rotation, it "scans" from t_1 to t_9 and back. The "there-and-back-again" form of the tap gains produces various cyclic vibrato effects.

3. SCANNER MODEL

In this section, we propose a simplified model of the scanner. Since the scanner capacitances are small compared to the ladder capacitors, it is reasonable to assume that they don't load the ladder circuit. Therefore, we are justified in modeling the LC ladder and scanner separately. The scanner takes the 19 node voltages $v_1 \cdots v_{19}$ as input and produces a single output voltage v_{out}.

At any given time, two plates overlap the rotor plate, creating two distinct capacitors. We assume that only these two capacitors have a non-negligible contribution to the output voltage. Under that assumption, those two form a capacitive voltage divider. To reflect this, we model the scanner output as a crossfade between two node voltages v_α and v_β according to $v_{\text{out}} = \eta\, v_\alpha + (1-\eta)v_\beta$. The mixing coefficient $\eta \in [0.0, 1.0]$ varies with the two capacitances C_α and C_β as $\eta = C_\alpha/(C_\alpha + C_\beta)$. Assuming circular symmetry of each plate and ignoring the small gap between stacks, $C_\alpha + C_\beta$ is a constant. Since each capacitance is theoretically proportional to the overlap area, the gain is modeled as a simple function of the rotor angle, according to Fig. 3. The variation of rotor angle over time follows the one in the physical organ, where the rotor is driven at a constant rate of ≈ 6 Hz by a synchronous motor [3].

4. WDF MODEL OF LC LADDER

In this section, we detail WDF simulation of the LC ladder circuit. The structure for subcircuits two, three, and four is outlined in Section 4.1. The first subcircuit contains multiple nonadaptable linear elements and cannot be handled with standard WDF techniques. We introduce a new approach to resolving this issue in Section 4.2 and apply it to the LC ladder in Section 4.3. In Section 4.4 we use the frequency-warped bilinear transform for WDF discretization of capacitors and inductors; in Section 4.5 we review WDF polarity inverters which are essential for proper bookkeeping.

4.1. WDF Tree (Subcircuits 2–4)

To model the LC ladder circuit, we derive the WDF structure of its circuit. Fig. 4 shows the partitioned schematic rearranged to highlight the underlying topology (with polarities labeled) and Fig. 5 shows the resulting WDF structure.

The 6 stages in the second subcircuit can be decomposed into standard WDF one-ports (R_{x-}, R_{x+}, L_x, and C_x) and adaptors ($\mathcal{S}_x$, $\mathcal{S}_{x\prime}$, $\mathcal{P}_x$, and $\mathcal{P}_{x\prime}$). The presence of the two inverters $\mathcal{I}_x$ and $\mathcal{I}_{x\prime}$ warrants explanation. We have already assigned polarities to the ports that connect stages, and series and parallel adaptors have inherent port polarities. Inverters $\mathcal{I}_x$ reconcile the discrepancy between the polarity of the right-facing port of each parallel adaptor $\mathcal{P}_x$ and the left-facing port of $\mathcal{P}_{(x+1)\prime}$ or $\mathcal{S}_7$. Inverters $\mathcal{I}_{x\prime}$ simplify the extraction of node voltages v_x, which are calculated by combining port voltages across resistors R_c and R_{x-} as

$$v_x = v_c + v_{x-} = \frac{1}{2}\left(a_c + b_c + a_{x-} + b_{x-}\right), \qquad (1)$$

where v_c, a_c, and b_c are the port voltage across, incident wave, and reflected wave at resistor R_c in the first subcircuit.

The 12 stages in the third subcircuit can be decomposed into standard WDF one-ports (L_y and C_y) and adaptors ($\mathcal{S}_y$ and $\mathcal{P}_y$). Again inverters $\mathcal{I}_y$ reconcile the discrepancy between the polarity of the right-facing port of each $\mathcal{P}_y$ and the left-facing port of $\mathcal{S}_{y+1}$ or R_t. Node voltages v_y in this subcircuit are extracted by combining the port voltages of resistor R_c and the left-facing port voltage of each stage $v_{y,l}$ as

$$v_y = v_c + v_{y,l} = \frac{1}{2}\left(a_c + b_c + a_{y,l} + b_{y,l}\right). \qquad (2)$$

The fourth subcircuit is decomposed simply into a WDF resistor R_t. Node voltage v_{19} is extracted by

$$v_{19} = v_c + v_t = \frac{1}{2}\left(a_c + b_c + a_t + b_t\right). \qquad (3)$$

4.2. Root with Multiple Elements

Reference circuits such as the Hammond organ vibrato/chorus circuit commonly include multiple nonadaptable elements (linear and nonlinear). Trying to accomodate multiple nonadaptable elements in a standard WDF connection tree causes unavoidable delay-free loops which leads to computability problems.

Historically, algorithm designers commonly use one of two tactics to ameliorate these issues. One tactic is to alter the reference circuit to make the structure computable. It is common to approximate ideal voltage sources as resistive voltage sources with small series resistances and to approximate ideal current sources as resistive current sources with large parallel resistances. The same principle can be used to approximate short circuits or the closed state of switches as small resistances and to approximate open circuits or the open state of switches as large resistances. Furthermore, certain nonlinear elements can be reasonably approximated by linearizing them with controlled sources and immittances [6,23]. A second tactic is to alter the WDF by introducing fictitious unit delays to resolve delay-free loops. Fettweis used this approach [5] before developing reflection-free ports [24], and it is still common in virtual analog [25, 26]. Of course, altering the reference circuit through these tactics introduces error (e.g. dissipation, dispersion) and can have adverse effects on stability.
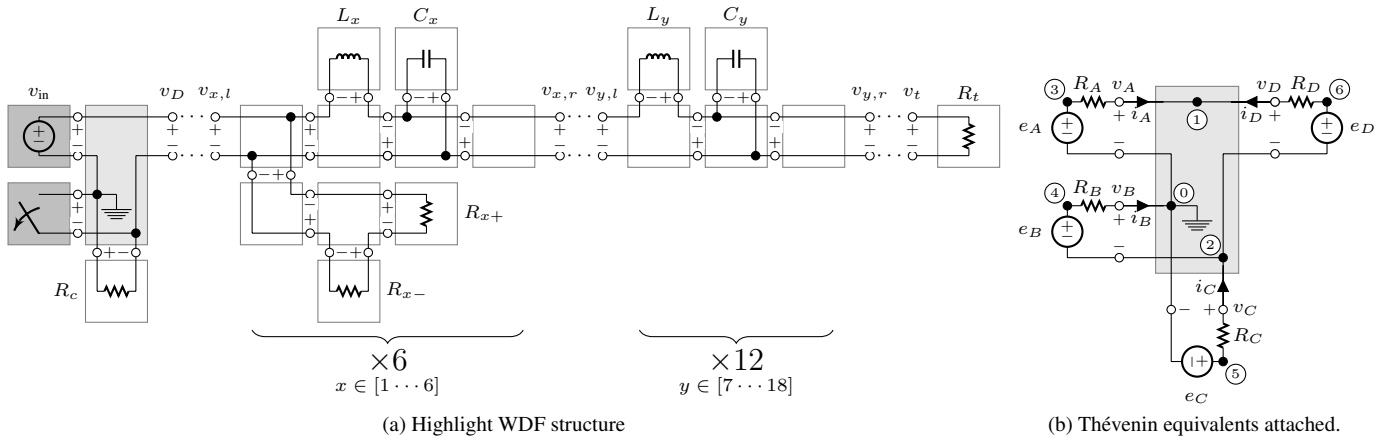
(a) Highlight WDF structure

(b) Thévenin equivalents attached.

Figure 4: *LC ladder Schematic, rearranged towards WDF.*
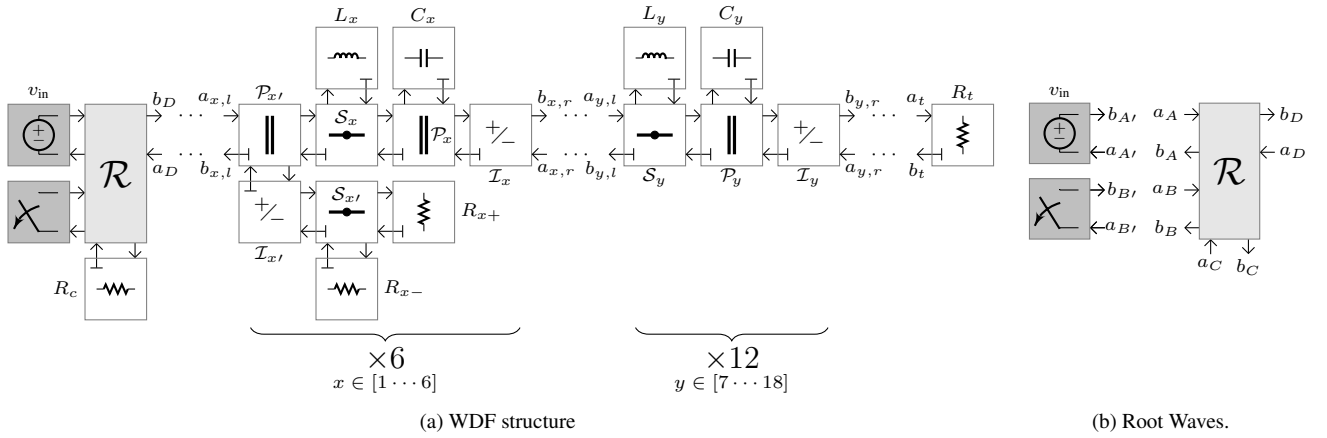

(a) WDF structure

(b) Root Waves.

Figure 5: *WDF structure of LC ladder.*

In [8], Werner *et al.* propose a method for handling multiple nonlinearities that does not resort to these tactics. All of the non-linearities are grouped as sub-elements of a WDF structure at the root of the WDF tree. Inside that structure, and after proper modification of the circuit graph, those elements end up being connected to each other through a complex $\mathcal{R}$-type adaptor that also interfaces those elements to the rest of the circuit. The method of [27] is used to solve for the scattering behavior of this $\mathcal{R}$-type adaptor. Because of the non-adaptable nature of the root elements, the response of the root adaptor structure from the perspective of the rest of the tree forms an implicit loop that we can resolve using either a tabulated solution [8] or an iterative solution [28, 29]. These approaches extends readily to nonadaptable linear elements, but is unnecessarily complex. Here we propose a novel more efficient approach for the case of multiple nonadaptable linear elements.

Consider a complex root topology with "external" incident waves $\boldsymbol{a}_e$ and reflected waves $\boldsymbol{b}_e$ facing the rest of the circuit and "internal" incident waves $\boldsymbol{a}_i$ and reflected waves $\boldsymbol{b}_i$ facing the non-adaptable linear elements, related by the scattering relationship

$$\begin{bmatrix} \boldsymbol{b}_i \\ \boldsymbol{b}_e \end{bmatrix} = \begin{bmatrix} \mathbf{S}_{11} & \mathbf{S}_{12} \\ \mathbf{S}_{21} & \mathbf{S}_{22} \end{bmatrix} \begin{bmatrix} \boldsymbol{a}_i \\ \boldsymbol{a}_e \end{bmatrix} \tag{4}$$

The vector of nonadaptable linear elements relates the incident

waves $\boldsymbol{a}_{\text{root}}$ and inputs $\boldsymbol{x}_{\text{root}}$ to reflected waves $\boldsymbol{b}_{\text{root}}$ by

$$\boldsymbol{b}_{\text{root}} = \boldsymbol{\Phi} \boldsymbol{a}_{\text{root}} + \boldsymbol{\Psi} \boldsymbol{x}_{\text{root}} , \tag{5}$$

where $\boldsymbol{\Phi}$ and $\boldsymbol{\Psi}$ embody the wave-domain behavior of the linear elements. $\boldsymbol{a}_{\text{root}}$ and $\boldsymbol{b}_{\text{root}}$ are related to the $\boldsymbol{a}_i$ and $\boldsymbol{b}_i$ by

$$\boldsymbol{a}_{\text{root}} = \boldsymbol{b}_i \quad \text{and} \quad \boldsymbol{a}_i = \boldsymbol{b}_{\text{root}} . \tag{6}$$

Combining (4), (5), and (6) and solving for $\boldsymbol{b}_e$ yields

$$\boldsymbol{b}_e = \boldsymbol{\Gamma} \boldsymbol{a}_e + \boldsymbol{\Theta} \boldsymbol{x}_{\text{root}} \quad \text{with}$$
$$\boldsymbol{\Gamma} = \boldsymbol{\Theta} \mathbf{S}_{12} + \mathbf{S}_{22} , \quad \boldsymbol{\Theta} = \mathbf{S}_{21} \left(\mathbf{I} - \boldsymbol{\Phi} \mathbf{S}_{11} \right)^{-1} \boldsymbol{\Psi} , . \tag{7}$$

4.3. WDF Root (Subcircuit 1)

Here, we apply the theory developed in Section 4.2 to the first subcircuit of the Hammond vibrato/chorus. The first subcircuit contains two non-adaptable elements, a voltage source and a switch. As a result, those two elements need to be grouped at the root of the WDF structure following the method outlined in Section 4.2, connecting them through an $\mathcal{R}$-type adaptor [27] with incident and reflected waves

$$\boldsymbol{a} = \begin{bmatrix} \boldsymbol{a}_i^\top & \boldsymbol{a}_e^\top \end{bmatrix}^\top \quad \text{and} \quad \boldsymbol{b} = \begin{bmatrix} \boldsymbol{b}_i^\top & \boldsymbol{b}_e^\top \end{bmatrix}^\top , \tag{8}$$

$$
\begin{array}{c}
 \\
\textcircled{0} \\
\textcircled{1} \\
\textcircled{2} \\
\textcircled{3} \\
\textcircled{4} \\
\textcircled{5} \\
\textcircled{6} \\
A \\
B \\
C \\
D
\end{array}
\begin{bmatrix}
G_B & 0 & 0 & 0 & -G_B & 0 & 0 & -1 & 0 & -1 & 0 \\
0 & G_A+G_D & 0 & -G_A & 0 & 0 & -G_D & 0 & 0 & 0 & -1 \\
0 & 0 & G_C & 0 & 0 & -G_C & 0 & 0 & -1 & 0 & 0 \\
0 & -G_A & 0 & G_A & 0 & 0 & 0 & 1 & 0 & 0 & 0 \\
-G_B & 0 & 0 & 0 & G_B & 0 & 0 & 0 & 1 & 0 & 0 \\
0 & 0 & -G_C & 0 & 0 & G_C & 0 & 0 & 0 & 1 & 0 \\
0 & -G_D & 0 & 0 & 0 & 0 & G_D & 0 & 0 & 0 & 1 \\
-1 & 0 & 0 & 1 & 0 & 0 & 0 & 0 & 0 & 0 & 0 \\
0 & 0 & -1 & 0 & 1 & 0 & 0 & 0 & 0 & 0 & 0 \\
-1 & 0 & 0 & 0 & 1 & 0 & 0 & 0 & 0 & 0 & 0 \\
0 & -1 & 0 & 0 & 0 & 0 & 1 & 0 & 0 & 0 & 0
\end{bmatrix}
\begin{bmatrix}
v_{\textcircled{0}} \\ v_{\textcircled{1}} \\ v_{\textcircled{2}} \\ v_{\textcircled{3}} \\ v_{\textcircled{4}} \\ v_{\textcircled{5}} \\ v_{\textcircled{6}} \\ j_A \\ j_B \\ j_C \\ j_D
\end{bmatrix}
=
\begin{bmatrix}
0 \\ 0 \\ 0 \\ 0 \\ 0 \\ 0 \\ 0 \\ e_A \\ e_B \\ e_C \\ e_D
\end{bmatrix}
$$

Figure 6: MNA matrix. Red and blue cells respectively show examples of resistor and voltage source "stamps" [27].

"external" wave vectors

$$\boldsymbol{a}_e = \begin{bmatrix} a_C & a_D \end{bmatrix}^\top \quad \text{and} \quad \boldsymbol{b}_e = \begin{bmatrix} b_C & b_D \end{bmatrix}^\top, \qquad (9)$$

and "internal" wave vectors

$$\boldsymbol{a}_i = \begin{bmatrix} a_A & a_B \end{bmatrix}^\top \quad \text{and} \quad \boldsymbol{b}_i = \begin{bmatrix} b_A & b_B \end{bmatrix}^\top. \qquad (10)$$

Using the method of [27], we can solve for the scattering matrix $\mathbf{S}$ that relates the incident waves $\boldsymbol{a}$ and reflected waves $\boldsymbol{b}$ as $\boldsymbol{b} = \mathbf{S}\boldsymbol{a}$. To do so, we attach instantaneous Thévenin port equivalents to each of the ports $A \cdots D$ (Fig. 4b) and confront Modified Nodal Analysis (the MNA system for Fig. 4b is shown in Fig. 6) with the standard voltage wave definition, yielding

$$\mathbf{S} = \mathbf{I} + 2 \begin{bmatrix} \mathbf{0} & \mathbf{R} \end{bmatrix} \mathbf{X}^{-1} \begin{bmatrix} \mathbf{0} & \mathbf{I} \end{bmatrix}^\top \qquad (11)$$

where $\mathbf{R} = \mathrm{diag}\left(\begin{bmatrix} R_A \cdots R_D \end{bmatrix}\right)$ is the diagonal matrix of port resistances and $\mathbf{X}$ is the MNA system matrix.

The vector of nonadaptable linear elements includes the voltage source v_{in} and the switch, which relate "root" wave vectors

$$\boldsymbol{a}_{\text{root}} = \begin{bmatrix} a_{A'} & a_{B'} \end{bmatrix}^\top \quad \text{and} \quad \boldsymbol{b}_{\text{root}} = \begin{bmatrix} b_{A'} & b_{B'} \end{bmatrix}^\top. \qquad (12)$$

As before, port connections enforce $\boldsymbol{a}_{\text{root}} = \boldsymbol{b}_i$ and $\boldsymbol{a}_i = \boldsymbol{b}_{\text{root}}$.

The ideal voltage source v_{in} has the wave-domain relationship

$$b_{A'}[n] = a_{A'}[n] + 2\,v_{\text{in}}[n]. \qquad (13)$$

An ideal switch has the wave-domain relationship

$$b_{B'}[n] = w\,a_{B'}[n], \quad w = \begin{cases} -1 & \text{open switch} \\ +1 & \text{closed switch} \end{cases}. \qquad (14)$$

In the context of (5), (13)–(14) define

$$\boldsymbol{\Phi} = \begin{bmatrix} -1 & 0 \\ 0 & w \end{bmatrix}, \quad \boldsymbol{\Psi} = \begin{bmatrix} 2 & 0 \\ 0 & 0 \end{bmatrix}, \quad \boldsymbol{x}_{\text{root}} = \begin{bmatrix} v_{\text{in}} \\ 0 \end{bmatrix}. \qquad (15)$$

Plugging (15) and (11) into (7) yields $\boldsymbol{b}_e$, solving the root topology with multiple nonadaptable linear elements.

4.4. Frequency-Warped One-Port Linear Reactances

Having solved the issue of realizing the WDF, we now turn our attention to discretization schemes for its reactances. The LC ladder's 36 reactances combine to create magnitude responses with numerous salient features, especially a sharp lowpass cutoff. To control the magnitude response's match to the reference domain, we apply the well-known frequency-warped bilinear transform to the wave-digital capacitor and inductor.

WDFs involve one-port ideal linear reactances: the capacitor (of capacitance C) and inductor (of inductance L). Their current–voltage relationships are:

$$C\dot{v}(t) = i(t) \quad \text{and} \quad v(t) = L\dot{i}(t) \qquad (16)$$

where v is the port voltage, and i is the port current. Their corresponding Laplace transforms are:

$$Cs\mathcal{V}(s) = \mathcal{I}(s) \quad \text{and} \quad \mathcal{V}(s) = Ls\mathcal{I}(s). \qquad (17)$$

Plugging in the standard WDF voltage-wave definitions

$$a = v + Ri \quad \text{and} \quad b = v - Ri \qquad (18)$$

parameterized by arbitrary port resistance R yields continuous-time transfer functions $\mathcal{H}(s) = \mathcal{B}(s)/\mathcal{A}(s)$:

$$\mathcal{H}_C(s) = \frac{1 - RCs}{1 + RCs} \quad \text{and} \quad \mathcal{H}_L(s) = \frac{R - Ls}{R + Ls} \qquad (19)$$

To simulate the system, we discretize reactive elements to obtain $H(z^{-1}) = B(z^{-1})/A(z^{-1})$ for each. WDFs commonly use the bilinear transform (BLT) [4], which substitutes $\frac{2}{T}\frac{1-z^{-1}}{1+z^{-1}}$ for s in $\mathcal{H}(s)$ to form $H(z^{-1})$ (T is the sampling period). The BLT's desirable numerical properties include transfer function order preservation, unconditional stability, and passivity in the WDF domain, but it suffers from a well-known frequency distortion [18].

A common extension to the BLT is the warped (or generalized) BLT which is identical except T is replaced by T' [30] so as to substitute $\frac{2}{T'}\frac{1-z^{-1}}{1+z^{-1}}$ for s. This degree of freedom is used to alter the BLT's frequency distortion and ensure that, by selecting T' properly, one continuous-time frequency Ω_0 is mapped correctly, i.e., $\mathcal{H}(j\Omega_0) = H(e^{-j\Omega_0 T})$. The coefficient T' that achieves the correct mapping is given by:

$$T' = 2\tan\left(\Omega_0 T/2\right)/\Omega_0. \qquad (20)$$

The warped BLT has the same desirable numerical properties as the BLT. Since it is not common in the WDF context, we briefly develop warped BLT discretization of WDF one-port reactances.

One-port linear reactances have a first-order continuous-time transfer function, so the warped BLT yields a first-order transfer function in discrete time with z-transform

$$H(z^{-1}) = \frac{B(z^{-1})}{A(z^{-1})} = \frac{\beta_0 + \beta_1 z^{-1}}{\alpha_0 + \alpha_1 z^{-1}}. \qquad (21)$$

For a capacitor C and inductor L, these coefficients are:

$$C: \quad \beta_0 = \alpha_1 = \frac{T'}{2C} - R \quad , \quad \beta_1 = \alpha_0 = \frac{T'}{2C} + R \qquad (22)$$

$$L: \quad \beta_0 = -\alpha_1 = R + \frac{2L}{T'} \quad , \quad \beta_1 = -\alpha_0 = R - \frac{2L}{T'} . \quad (23)$$

To eliminate delay-free loops, all one-port leaf elements of a WDF require *adaptation*: picking a value of R that satisfies $\beta_0 = 0$. The port impedances that adapt a capacitor and inductor are

$$R_C = T'/(2C) \quad \text{and} \quad R_L = 2L/T' \qquad (24)$$

which yield discretized transfer functions

$$H_C(z^{-1}) = z^{-1} \quad \text{and} \quad H_L(z^{-1}) = -z^{-1} . \qquad (25)$$

Interestingly, the discretized transfer functions of the capacitor and inductor do not depend on C, L, or T'. However, all of these *do* affect their adapted port resistance.

(a) Kirchhoff domain.   (b) Wave domain.
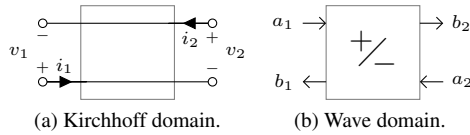
Figure 7: *WDF 2-port series adaptor / inverter.*

4.5. Wave-Digital Inverter

We saw above that wave-digital polarity inverters must necessarily be employed for proper bookkeeping of port connection polarity and to simplify the calculation of node voltages. Here, we review the derivation of those inverters.

Consider two connected ports 1 and 2 with port voltages v_1 and v_2 and port currents i_1 and i_2; these ports can be connected in two ways. In the Kirchhoff domain, a two-port parallel connection is characterized by $v_1 = v_2$ and $i_1 = -i_2$ and a two-port series connection by $i_1 = i_2$ and $v_1 = -v_2$. Plugging in the standard WDF voltage wave definition (18) yields a scattering relationship

$$\begin{bmatrix} b_1 \\ b_2 \end{bmatrix} = \underbrace{\begin{bmatrix} s_{11} & s_{12} \\ s_{21} & s_{22} \end{bmatrix}}_{\mathbf{S}} \begin{bmatrix} a_1 \\ a_2 \end{bmatrix} , \qquad (26)$$

parameterized by the two port resistances R_1 and R_2. These two-port adaptors scatter according to

$$\mathbf{S} = \begin{bmatrix} -\frac{R_1 - R_2}{R_1 + R_2} & \frac{2\lambda R_1}{R_1 + R_2} \\ \frac{2\lambda R_2}{R_1 + R_2} & \frac{R_1 - R_2}{R_1 + R_2} \end{bmatrix} , \quad \lambda = \begin{cases} -1 & \text{series} \\ +1 & \text{parallel} \end{cases} \qquad (27)$$

and are both rendered reflection-free by setting $R_1 = R_2$:

$$\begin{bmatrix} s_{11} & s_{12} \\ s_{21} & s_{22} \end{bmatrix} = \begin{bmatrix} 0 & \lambda \\ \lambda & 0 \end{bmatrix} . \qquad (28)$$

Notice that the reflection-free two-port parallel connection is simply a normal WDF port connection [4] with each incident wave equal to the opposite reflected wave. The two-port series connection inverts the reflected wave from each port to form the incident wave at the other port; it is in fact the wave-digital inverter (Fig. 7) [27, 31].

5. RESULTS

Here we discuss some results that characterize our model of the Hammond vibrato/chorus, including the impulse and magnitude responses of each tap in the LC ladder (Section 5.1), a study on the spectral aspects of scanner interpolation (Section 5.2), and the response to a single sinusoid (Section 5.3). These results reveal a variety of effects, including delay-length modulation, phaser-like effects, amplitude modulation, and modulated comb filter effects.

5.1. Impulse and Magnitude Responses of LC Ladder

Figs. 8 and 9 show the impulse and magnitude responses at each tap $v_1 \cdots v_{19}$ under two different WDF discretizations compared to a reference "ground truth" SPICE simulation.

In Fig. 8, we use a sampling rate of $f_s = 44100$ Hz, with the capacitors and inductors discretized using the standard BLT with no frequency warping, i.e., $T' = T = 1/f_s \approx 2.2676 \times 10^{-5}$. In Fig. 9, use use instead a warped BLT with T' chosen to match the frequency $\Omega_0 = 7075$ Hz, approximately the passband edge of the ladder, yielding $T' \approx 2.2724 \times 10^{-5}$ (20).

In the time domain plots, it can be seen that the LC ladder approximates a delay line. In theory, LC ladders have an idealized total delay time of $\sqrt{\sum L \times \sum C}$ [32], meaning ≈ 0.85 ms for the Hammond vibrato/chorus. It can be seen in the SPICE simulations that the impulse is delayed and "smeared" progressively as it travels down the line, and indeed experiences ≈ 0.85 ms of delay by tap 19. To understand the complex nature of this smearing, we turn to the magnitude response.

In the magnitude response, the lowpass characteristic of the LC ladder is apparent. In the SPICE simulations, the passband edge frequency is ≈ 7075 Hz. The amount of attenuation in the stopband depends on tap index: v_1 has no attenuation, and the slope increases as tap index increases. Notice that in the simulation using the unwarped BLT, dc is matched perfectly, while frequency distortion builds up as frequency increases. Specifically, the passband edge is depressed by almost 500 Hz compared to the SPICE simulation. Using the warped BLT, 7075 Hz is matched perfectly. While matching the passband edge may be preferable due to its perceptual salience, a mismatch remains for the rest of the magnitude response, most noticeably between dc and the passband edge. While the passband has *dozens* of features, the warped BLT can only match *one*. Notice that, back in the time domain, the frequency warpings of different discretizations manifests as different smearings. Alternatively, applying $4\times$ oversampling is an effective though expensive way to achieve good agreement from dc to the passband edge.

5.2. Magnitude Response of Scanner Model Interpolation

Fig. 10 shows the magnitude response of scanner model interpolation between terminals for the V1 (Fig. 10a), V2 (Fig. 10b), and V3 (Fig. 10c) settings (using the unwarped BLT). dB markings are shown on the color axis. The horizontal axis represents the scanner angle θ. At the vertical markings with tap indices labeled underneath, the scanner is exactly on one of the terminals. Between tap indices are interpolations between them.

In addition to providing a time-varying delay, the ladder circuit and scanner impart complex spectral coloration. First, the sharp passband edge is modulated slightly over the course of each vibrato cycle. The passband ripples also follow complex trajectories during each cycle. Since the ripples are relatively deep (many
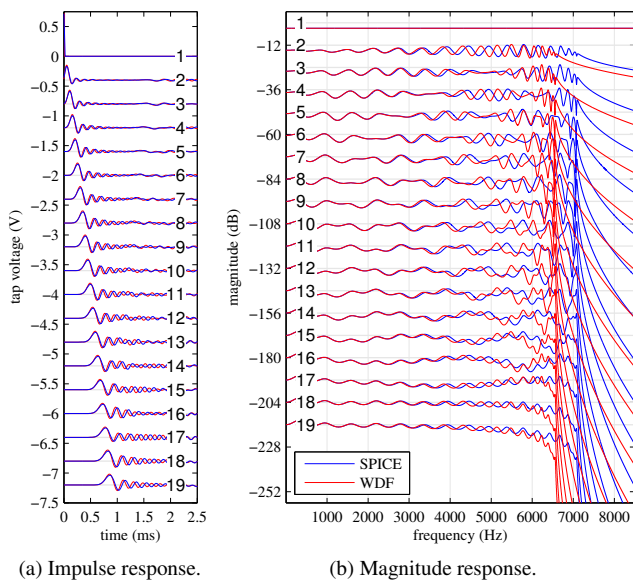
(a) Impulse response. (b) Magnitude response.

Figure 8: *Responses of the LC ladder, using unwarped BLT.*

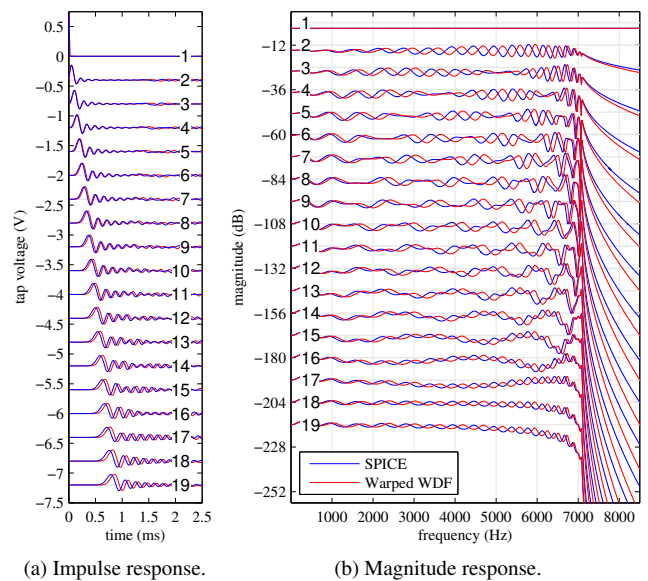

(a) Impulse response. (b) Magnitude response.

Figure 9: *Responses of the LC ladder, using warped BLT.*

around 6 dB and some larger), they create an audible phaser-like effect on broadband input signals. The voltage dividers R_{k-} and R_{k+}, $k \in 1 \cdots 6$, produce amplitude modulation during each cycle of θ [10]. Table 3 shows the gain of each stage's divider.

Table 3: *Voltage divider gains (in dB) at each tap.*

tap	1	2	3	4	5	6	7 ⋯ 19
gain	−2.9	−2.8	−2.0	−1.5	−0.83	−0.56	0

Since the Hammond vibrato/chorus approximates a delay line it is not surprising that the magnitude response of the scanner interpolation exhibits comb-filter-like features. Assuming the idealized delay time discussed earlier, linear interpolation would produce notches halfway through each crossfade at frequencies dictated by the separation between taps, at the locations indicated by × symbols. The actual minima in the Hammond response are very close to these notches, as predicted.

5.3. Sinusoid Study

We study a single 1760 Hz (A6 in scientific pitch notation) sinusoidal input for the three vibrato depth settings (Fig. 11). Notice that the V1 setting produces the narrowest vibrato, the V2 setting produces a medium vibrato, and the V3 setting produces the widest vibrato. Notice also that each setting produces a differently shaped vibrato. The vibrato width and shape are a consequence of the different tap spacings of each setting; the time-varying phase shift for a given frequency, which manifests as frequency modulation, is proportional to the time derivative of its group delay [19]. The combination of amplitude modulation and frequency modulation is visible as 6 × 16 Hz spaced sidebands around the main signal.

6. CONCLUSION

In this study on modeling the Hammond organ vibrato/chorus, we introduced new theoretical tools enabling the inclusion of multiple linear nonadaptable elements at the root of a WDF tree, applied the well-known frequency-warped bilinear transform to the derivation of wave-digital capacitors and inductors, and illustrated the systematic use of wave-digital polarity inverters. Although beyond the scope of this paper, the complex spectral properties and frequency-dependent vibrato of the Hammond organ vibrato/chorus deserve further study (cf. the complexities of vocal vibrato, including "spectral modulation" [33]).

7. ACKNOWLEDGMENTS

Thanks to Jonathan Abel for helpful discussions on ladder circuits.

8. REFERENCES

[1] "Service manual—models: A, A-100, AB, BA, BC, BCV, BV, B2, B3, C, CV, C2, C-2G, C3, D, DV, D-100, E, G, GV, RT, RT-2, RT-3," Tech. Rep. HOOO-OOO495, Nov. 1987.

[2] S. Hammond, "Analog Outfitters scanner review," *Premier Guitar*, Dec. 18 2015.

[3] J. M. Hanert, "Electrical musical apparatus," Aug. 14 1945, U.S. Patent No. 2,382,413.

[4] A. Fettweis, "Wave digital filters: Theory and practice," *Proc. IEEE*, vol. 74, no. 2, pp. 270–327, 1986.

[5] A. Fettweis, "Digital filters structures related to classical filter networks," *Archiv Elektronik Übertragungstechnik (AEÜ)*, vol. 25, pp. 79–89, 1971.

[6] G. De Sanctis and A. Sarti, "Virtual analog modeling in the wave-digital domain," *IEEE Trans. Audio, Speech, Language Process. (TASLP)*, vol. 18, no. 4, pp. 715–727, 2010.

[7] H. E. Meinema and W. C. Johnson, H. A. .and Laube Jr., "A new reverberation device for high fidelity systems," *J. Audio Eng. Soc. (JAES)*, vol. 9, no. 4, pp. 284–326, 1961.

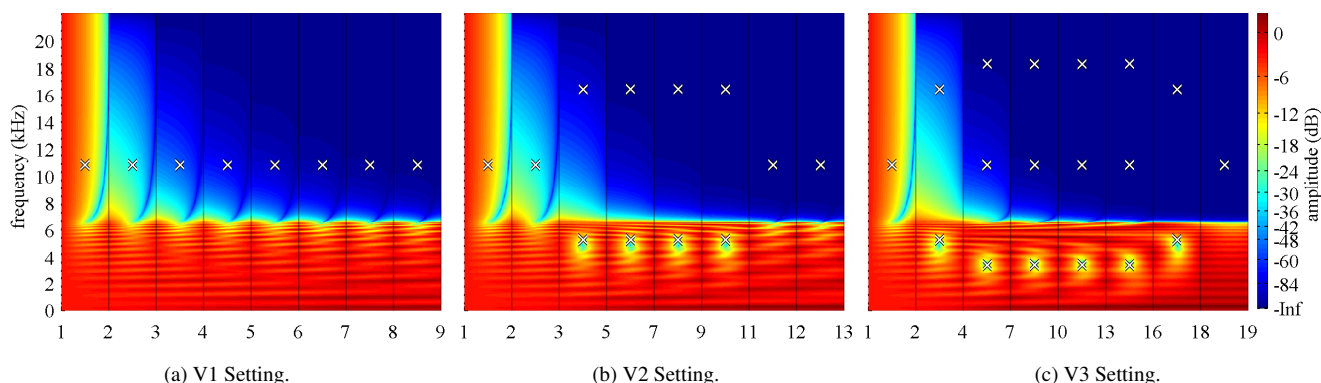(a) V1 Setting. (b) V2 Setting. (c) V3 Setting.

Figure 10: *Magnitude response at various interpolations. Recall Fig. 3 and Table 2.*

[8] K. J. Werner, V. Nangia, J. O. Smith III, and J. S. Abel, "Resolving wave digital filters with multiple/multiport nonlinearities," in *Proc. 18th Int. Conf. on Digital Audio Effects (DAFx)*, Trondheim, Norway, Nov. 30 – Dec. 3 2015.

[9] G. Reid, "Synthesizing tonewheel organs," *Sound on Sound (SOS)*, Nov. 2003.

[10] G. Reid, "Synthesizing Hammond organ effects: Part 1," *SOS*, Jan. 2004.

[11] J. Pekonen, T. Pihlajamäki, and V. Välimäki, "Computationally efficient Hammond organ synthesis," in *Proc. 14th DAFx*, Paris, France, Sept. 19–23 2011.

[12] K. J. Werner and J. S. Abel, "Modal processor effects inspired by Hammond tonewheel organs," *Appl. Sci.*, vol. 6, no. 7 (Special Issue "Audio Signal Processing"), 2016.

[13] J. S. Abel and K. J. Werner, "Distortion and pitch processing using a modal reverb architecture," in *Proc. 18th DAFx*, Trondheim, Norway, Nov. 30 – Dec. 3 2015.

[14] J. S. Abel, S. Coffin, and K. S. Spratt, "A modal architecture for artificial reverberation with application to room acoustics modeling," in *Proc. 137th AES*, Los Angeles, CA, Oct. 9–12 2014.

[15] D. J. Leslie, "Rotatable tremulant sound producer," Nov. 29 1949, U.S. Patent No. 2,489,653.

[16] R. Kronland-Martinet and T. Voinier, "Real-time perceptual simulation of moving sources: Application to the Leslie cabinet and 3D sound immersion," *EURASIP J. Audio, Speech, Music Process.*, 2008, Article ID 849696.

[17] J. Smith, S. Serafin, J. Abel, and D. Berners, "Doppler simulation and the Leslie," in *Proc. 5th DAFx*, Hamburg, Germany, Sept. 26–28 2002.

[18] J. O. Smith III, *Physical Audio Signal Processing for Virtual Musical Instruments and Audio Effects*, Online book, 2010 edition.

[19] S. Disch and U. Zölzer, "Modulation and delay line based digital audio effects," in *Proc. 2nd DAFx*, Trondheim, Norway, Dec. 9–11 1999.

[20] P. Dutilleux, M. Holters, S. Disch, and U. Zölzer, *Modulators and demodulators*, chapter 3, pp. 83–99, 2011, appears in [34].

[21] J. Herrera, C. Hanson, and S. Abel, J. "Discrete time emulation of the Leslie speaker," in *Proc. 127th Conv. Audio Eng. Soc. (AES)*, New York, NY, USA, Oct. 9–12 2009, Conv. Paper 7925.

[22] J. Dattorro, "Effect design part 2: Delay-line modulation and chorus," *JAES*, vol. 45, no. 10, pp. 764–768, Oct. 1997.

[23] K. J. Werner, W. R. Dunkel, M. Rest, M. J. Olsen, and J. O. Smith III, "Wave digital filter modeling of circuits with operational amplifiers," in *Proc. European Signal Process. Conf. (EUSIPCO)*, Budapest, Hungary, Aug. 29 – Sept. 2 2016.

[24] A. Fettweis and K. Meerkötter, "On adaptors for wave digital filters," *IEEE Trans. Acoust., Speech, Signal Process.*, vol. 23, no. 6, 1975.

[25] R. C. D. de Paiva, J. Pakarinen, V. Välimäki, and M. Tikander, "Real-time audio transformer emulation for virtual tube amplifiers," *EURASIP J. Advances Signal Process.*, 2011.
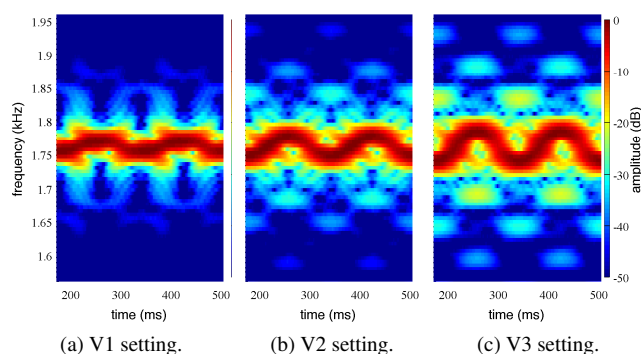
(a) V1 setting. (b) V2 setting. (c) V3 setting.

Figure 11: *Studying a single* 1760 *Hz sinusoid.*

[26] J. Pakarinen and M. Karjalainen, "Enhanced wave digital triode model for real-time tube amplifier emulation," *IEEE TASLP*, vol. 18, no. 4, pp. 738–746, 2010.

[27] K. J. Werner, J. O. Smith III, and J. S. Abel, "Wave digital filter adaptors for arbitrary topologies and multiport linear elements," in *Proc. 18th DAFx*, Trondheim, Norway, Nov. 30 – Dec. 3 2015.

[28] M. J. Olsen, K. J. Werner, and J. O. Smith III, "An iterative approach to resolving wave digital filters with grouped nonlinearities," in *Proc. 19th DAFx*, Brno, Czech Republic, Sept. 5–9 2016.

[29] W. R. Dunkel, M. Rest, K. J. Werner, M. J. Olsen, and J. O. Smith III, "The Fender Bassman 5F6-A family of preamplifier circuits—a wave digital filter case study," in *Proc. 19th DAFx*, Brno, Czech Republic, Sept. 5–9.

[30] F. G. Germain and K. J. Werner, "Design principles for lumped model discretization using Möbius transforms," in *Proc. 18th DAFx*, Trondheim, Norway, Nov. 30 – Dec. 3 2015.

[31] S. D'Angelo and V. Välimäki, "Wave-digital polarity and current inverters and their application to virtual analog audio processing," in *IEEE Int. Conf. Acoust. Speech Signal Process. (ICASSP)*, Kyoto, Japan, Mar. 2012, pp. 469–472.

[32] Rhombus Industries Inc., "Passive delay line design considerations," Tech. Rep. APP1_PAS, Huntington Beach, CA, Jan. 1998.

[33] R. Maher and J. Beauchamp, "An investigation of vocal vibrato for synthesis," *Appl. Acoust.*, vol. 30, pp. 219–245, 1990.

[34] U. Zölzer, Ed., *DAFX: Digital Audio Effects*, John Wiley & Sons, second edition, 2011.